Static And Fatigue Tensile Properties of High-Strength Polyacrylonitrile (PAN)-Based Carbon And Electrical-Class Glass Hybrid Fiber-Reinforced Epoxy Matrix Composites

Kimiyoshi Naito (NAITO.Kimiyoshi@nims.go.jp)
National Institute for Materials Science

Research Article

Keywords: Hybrid, Tensile property, Weibull modulus, Fatigue property, S–N curve, Stiffness reduction.

Posted Date: September 24th, 2021

DOI: https://doi.org/10.21203/rs.3.rs-915808/v1

Static and fatigue tensile properties of high-strength polyacrylonitrile (PAN)-based carbon and electrical-class glass hybrid fiber-reinforced epoxy matrix composites

Kimiyoshi Naito[1,2, *]

[1]National Institute for Materials Science, Polymer Matrix Hybrid Composite Materials Group, Tsukuba, 305-0047, Japan
[2]Tohoku University, Department of Aerospace Engineering, Sendai, 980-8579, Japan
[*]NAITO.Kimiyoshi@nims.go.jp

ABSTRACT

The static and fatigue tensile properties of high-strength polyacrylonitrile (PAN)-based carbon (IMS60) and electronic (E)-class glass (E-glass) hybrid fiber-reinforced epoxy matrix composites (HFRPs) were investigated. The fiber orientations of the HFRP specimens were set to unidirectional with $[(0_{(IMS60)})/(0_{(E\text{-}glass)})]_S$ (subscript S means symmetry and $[(0_{(IMS60)})/(0_{(E\text{-}glass)})/(0_{(E\text{-}glass)})/(0_{(IMS60)})]$), $[(0_{(E\text{-}glass)})/(0_{(IMS60)})]_S$, $[(0_{(E\text{-}glass)})/(0_{(IMS60)})_2]_S$, $[(0_{(E\text{-}glass)})/(0_{(IMS60)})_3]_S$, $[(0_{(E\text{-}glass)})/(0_{(IMS60)})_5]_S$, $[(0_{(E\text{-}glass)})_2/(0_{(IMS60)})]_S$, $[(0_{(E\text{-}glass)})_3/(0_{(IMS60)})]_S$, and $[(0_{(E\text{-}glass)})_5/(0_{(IMS60)})]_S$. Under static loading for the $[(0_{(IMS60)})/(0_{(E\text{-}glass)})]_S$, $[(0_{(E\text{-}glass)})/(0_{(IMS60)})]_S$, $[(0_{(E\text{-}glass)})/(0_{(IMS60)})_2]_S$, $[(0_{(E\text{-}glass)})/(0_{(IMS60)})_3]_S$, and $[(0_{(E\text{-}glass)})/(0_{(IMS60)})_5]_S$ HFRP specimens, the stress applied to the specimen was almost linearly proportional to the strain until failure. However, the tensile stress–strain curves of the $[(0_{(E\text{-}glass)})_2/(0_{(IMS60)})]_S$, $[(0_{(E\text{-}glass)})_3/(0_{(IMS60)})]_S$, and $[(0_{(E\text{-}glass)})_5/(0_{(IMS60)})]_S$ HFRP specimens had a complicated shape (jagged trace). The Weibull statistical distributions of the tensile strength values were also examined. The Weibull moduli for the $[(0_{(E\text{-}glass)})/(0_{(IMS60)})]_S$, $[(0_{(E\text{-}glass)})/(0_{(IMS60)})_2]_S$, $[(0_{(E\text{-}glass)})/(0_{(IMS60)})_3]_S$, $[(0_{(E\text{-}glass)})/(0_{(IMS60)})_5]_S$, $[(0_{(E\text{-}glass)})_2/(0_{(IMS60)})]_S$, $[(0_{(E\text{-}glass)})_3/(0_{(IMS60)})]_S$, and $[(0_{(E\text{-}glass)})_5/(0_{(IMS60)})]_S$ HFRP specimens were higher than those for the mono carbon fiber-reinforced epoxy (CFRP) and glass fiber-reinforced epoxy (GFRP) specimens. Under fatigue loading, the fatigue properties of the HFRP specimens showed CFRP-dominant behaviour at high stress levels and GFRP-dominant behaviour at low stress levels. The fatigue properties of the HFRP specimens increased with increasing volume fraction of CFRP in the following order: ($[(0_{(E\text{-}glass)})/(0_{(IMS60)})_5]_S$ > $[(0_{(E\text{-}glass)})/(0_{(IMS60)})_3]_S$ > $[(0_{(E\text{-}glass)})/(0_{(IMS60)})_2]_S$ > $[(0_{(IMS60)})/(0_{(E\text{-}glass)})]_S$ > $[(0_{(E\text{-}glass)})/(0_{(IMS60)})]_S$ > $[(0_{(E\text{-}glass)})_2/(0_{(IMS60)})]_S$ > $[(0_{(E\text{-}glass)})_3/(0_{(IMS60)})]_S$ > $[(0_{(E\text{-}glass)})_5/(0_{(IMS60)})]_S$).

Keywords: Hybrid; Tensile property; Weibull modulus; Fatigue property; *S–N* curve; Stiffness reduction.

Introduction

Fiber-reinforced polymer matrix composites (FRPs) have become a dominant material in the aerospace, high-performance automotive, and sporting goods industries[1,2]. By mixing two or more types of fibers in a common matrix to form a hybrid composite, it may be possible to create a material possessing the combined advantages of the individual composite.

Naito et al. characterized the tensile properties and fracture behavior of high-strength polyacrylonitrile (PAN)-based and high-modulus pitch-based hybrid carbon fiber-reinforced epoxy and polyimide matrix composites (CFRPs)[3–5]. The tensile stress–strain curves of the hybrid CFRP specimens showed a complicated shape (jagged trace). The hybrid composite can be considered one example of a material that prevents instantaneous failure.

A number of papers were written approximately 1970–1980 on the advantages and applications of hybrid composites, such as carbon/glass hybrid composites, under static loading[6–10]. This interest stems from a more cost-effective utilization of expensive fiber if it is used in hybrid form[11]. The development of fiber-hybrid composites is a logical evolution toward even more design freedom and hence more possibility for optimization and cost reduction[12]. Although fatigue behavior is an important property for many applications, the effects of hybridization on this property have not been extensively studied[13]. Wu et al.[14] reported the fatigue properties of hybrid composites. The addition of CFRP to a basalt fiber-reinforced polymer matrix composite increased the number of cycles to rupture of the hybrid composites. On the other hand, the addition of CFRP to a glass fiber-reinforced polymer matrix composite (GFRP) did not have the same effect. However, measuring the static and fatigue tensile failure of the same hybrid composites remains a challenging issue.

In the present work, static and fatigue tensile tests of high-strength PAN-based carbon (IMS60) and electronic (E)-class glass (E-glass) hybrid fiber-reinforced epoxy matrix composite (HFRP) specimens were performed to evaluate their potential. The Weibull statistical distributions of the static tensile strength and stiffness reduction during fatigue loading of the HFRP

specimens were also evaluated.

Results

Static tensile properties

Figure 1 shows typical tensile stress–strain (σ–ε) curves for the HFRP specimens. The results for the mono CFRP and GFRP specimens are also shown in this figure. For the mono $(0_{(IMS60)})_4$ CFRP and $(0_{(E\text{-}glass)})_4$ GFRP specimens, and $[(0_{(IMS60)})/(0_{(E\text{-}glass)})]_S$, $[(0_{(E\text{-}glass)})/(0_{(IMS60)})]_S$, $[(0_{(E\text{-}glass)})/(0_{(IMS60)})_2]_S$, $[(0_{(E\text{-}glass)})/(0_{(IMS60)})_3]_S$, and $[(0_{(E\text{-}glass)})/(0_{(IMS60)})_5]_S$ HFRP specimens, the stress applied to the specimens was almost linearly proportional to the strain until failure (the modulus, strength, and failure strain were defined as tensile modulus, E, tensile strength, σ_f, and failure strain, ε_f, respectively). However, the tensile stress–strain curves of the $[(0_{(E\text{-}glass)})_2/(0_{(IMS60)})]_S$, $[(0_{(E\text{-}glass)})_3/(0_{(IMS60)})]_S$, and $[(0_{(E\text{-}glass)})_5/(0_{(IMS60)})]_S$ HFRP specimens showed a complicated shape (jagged trace) [3–5]. For the IMS60 layers, the HFRP specimens showed an intermediate modulus in the initial stage of loading (this modulus was defined as the tensile modulus, E). The load reached its maximum (the strength and strain were defined as tensile strength, σ_f, and initial failure strain, ε_f, respectively). Subsequently, when the IMS60 layers began to fail, the high-ductility E-glass layers held the load, and the material continued to endure the load without instantaneous failure (this modulus was calculated for a constant strain range using a least square method and was defined as the secondary tensile modulus, E^*). Finally, the load reached its secondary maximum, and fracture of the HFRP specimen occurred (the strength and strain were defined as the secondary fracture strength, σ^*_f, and secondary failure strain, ε^*_f, respectively). Because higher ductility E-glass fibers could help the load for a certain time after failure occurred, HFRP specimens with jagged traces could be considered one example of a material able to prevent instantaneous failure[3–5]. The average tensile modulus (E), tensile strength (σ_f), failure strain (ε_f), secondary tensile modulus (E^*), strength (σ^*_f), and failure strain (ε^*_f) are shown in **Table 2**. Similar results of other hybrid composites have been observed in the reported literature[3–5].

Fatigue tensile properties

Figure 2 shows the relation between the applied maximum stress, σ_{max}, and the number of cycles to failure, N_f, also defined as the S–N curves for the HFRP specimens. The S–N curves for the mono CFRP and GFRP specimens are also shown in this figure. For the mono $(0_{(IMS60)})_4$ CFRP and $(0_{(E\text{-}glass)})_4$ GFRP specimens, the fatigue properties of the CFRP were ~2–4 times higher than those of the GFRP. The fatigue properties of the HFRP specimens showed CFRP-dominant behaviour at high stress levels and GFRP-dominant behaviour at low stress levels. The fatigue properties of the HFRP specimens increased with increasing volume fraction of CFRP ($[(0_{(E\text{-}glass)})/(0_{(IMS60)})_5]_S$ > $[(0_{(E\text{-}glass)})/(0_{(IMS60)})_3]_S$ > $[(0_{(E\text{-}glass)})/(0_{(IMS60)})_2]_S$ > $[(0_{(IMS60)})/(0_{(E\text{-}glass)})]_S$ > $[(0_{(E\text{-}glass)})/(0_{(IMS60)})]_S$ > $[(0_{(E\text{-}glass)})_2/(0_{(IMS60)})]_S$ > $[(0_{(E\text{-}glass)})_3/(0_{(IMS60)})]_S$ > $[(0_{(E\text{-}glass)})_5/(0_{(IMS60)})]_S$).

Discussion

The tensile modulus, E_{HFRP}, and secondary tensile modulus, E^*_{HFRP}, of the HFRP specimens were calculated using a simple rule of mixtures:

$$E_{HFRP} = E_{F(IMS60)}V_{F(IMS60)} + E_{F(E-glass)}V_{F(E-glass)} + E_M V_M \quad \text{(for tensile modulus)} \quad (1)$$

and

$$E^*_{HFRP} = E_{(E-glass)}V_{(E-glass)} \quad \text{(for secondary modulus)} \quad (2)$$

where $E_{F(IMS60)}$, $E_{F(E\text{-}glass)}$, E_M, and $E_{(E\text{-}glass)}$ are the tensile moduli of the IMS60 fiber, E-glass fiber, matrix, and E-glass GFRP, respectively. $V_{(E\text{-}glass)}$ is the volume fraction of E-glass GFRP. The volume fraction of each element is already known. The tensile modulus of the matrix is assumed to be E_M = 3.5 GPa. The tensile moduli of the mono CFRP and GFRP specimens are $E_{(IMS60)}$ = 159 GPa and $E_{(E\text{-}glass)}$ = 38 GPa, respectively. $E_{F(IMS60)}$ and $E_{F(E\text{-}glass)}$ are estimated from Eq. (1), and $E_{F(IMS60)}$ = 277 GPa and $E_{F(E\text{-}glass)}$ = 75 GPa.

The estimated tensile modulus (E_{cal}) and secondary tensile modulus (E^*_{cal}) are shown in **Table 3** and **Supplementary Fig. S1**. The experimental results of the tensile modulus and secondary tensile modulus of the HFRP specimens were in agreement with the rule of mixture prediction. Similar results of hybrid composites have been observed in the reported literature[15–17].

The tensile strength, $\sigma_{f(HFRP)}$, and secondary fracture strength, $\sigma^*_{f(HFRP)}$, of the HCFRP specimens were also calculated using the rule of mixtures:

$$\sigma_{f(HFRP)} = \sigma_{Ff(IMS60)}V_{F(IMS60)} + \frac{\sigma_{Ff(IMS60)}}{E_{F(IMS60)}}E_{F(E-glass)}V_{F(E-glass)} + \frac{\sigma_{Ff(IMS60)}}{E_{F(IMS60)}}E_M V_M \quad \text{(for tensile strength)} \quad (3)$$

$$\sigma_{f(HFRP)} = \sigma_{Ff(E-glass)}V_{F(E-glass)} + \frac{\sigma_{Ff(E-glass)}}{E_{F(E-glass)}}E_M V_M \quad \text{(for tensile strength)} \quad (4)$$

and

$$\sigma^*_{f(HFRP)} = \sigma_{f(E-glass)} V_{(E-glass)} \quad \text{(for secondary fracture strength)} \quad (5)$$

where $\sigma_{Ff(IMS60)}$, $\sigma_{Ff(E\text{-}glass)}$, and $\sigma_{f(E\text{-}glass)}$ are the tensile strength values of the IMS60 fiber, E-glass fiber, and E-glass GFRP, respectively. The volume fraction and tensile modulus of each element are already known. The tensile strength values of the mono CFRP and GFRP specimens are $\sigma_{f(IMS60)}$ = 3.023 GPa and $\sigma_{f(E\text{-}glass)}$ = 1.109 GPa, respectively. $\sigma_{Ff(IMS60)}$ and $\sigma_{Ff(E\text{-}glass)}$ are estimated from Eqs. (3), (4), and (5), and $\sigma_{Ff(IMS60)}$ = 5.279 GPa and $\sigma_{Ff(E\text{-}glass)}$ = 2.169 GPa.

The failure strain $\varepsilon_{f(HFRP)}$ and secondary failure strain $\varepsilon^*_{f(HFRP)}$ of the HCFRP specimens were calculated using the following equations:

$$\varepsilon_{f(HFRP)} = \frac{\sigma_{f(HFRP)}}{E_{HFRP}} \quad \text{(for failure strain)} \quad (6)$$

and

$$\varepsilon^*_{f(HFRP)} = \frac{\sigma^*_{f(HFRP)}}{E^*_{HFRP}} \quad \text{(for secondary failure strain)} \quad (7)$$

The estimated tensile strength ($\sigma_{f.cal}$), secondary fracture strength ($\sigma^*_{f.cal}$), failure strain ($\varepsilon_{f.cal}$), and secondary failure strain ($\varepsilon^*_{f.cal}$) are shown in **Table 3** and **Supplementary Fig. S2**.

The tensile strength values of the $[(0_{(E\text{-}glass)})/(0_{(IMS60)})]_S$, $[(0_{(E\text{-}glass)})/(0_{(IMS60)})_2]_S$, $[(0_{(E\text{-}glass)})_2/(0_{(IMS60)})]_S$, $[(0_{(E\text{-}glass)})_3/(0_{(IMS60)})]_S$, and $[(0_{(E\text{-}glass)})_5/(0_{(IMS60)})]_S$ HFRP specimens were higher than those of their predicted values. The secondary fracture strength values of the $[(0_{(E\text{-}glass)})_3/(0_{(IMS60)})]_S$ and $[(0_{(E\text{-}glass)})_5/(0_{(IMS60)})]_S$ HFRP specimens were higher than those of their predicted values. The secondary failure strains of the $[(0_{(E\text{-}glass)})_2/(0_{(IMS60)})]_S$, $[(0_{(E\text{-}glass)})_3/(0_{(IMS60)})]_S$, and $[(0_{(E\text{-}glass)})_5/(0_{(IMS60)})]_S$ HFRP specimens were similar to that of the E-glass GFRP specimen. However, the failure strains of the $[(0_{(E\text{-}glass)})/(0_{(IMS60)})]_S$, $[(0_{(E\text{-}glass)})/(0_{(IMS60)})_2]_S$, $[(0_{(E\text{-}glass)})_2/(0_{(IMS60)})]_S$, $[(0_{(E\text{-}glass)})_3/(0_{(IMS60)})]_S$, and $[(0_{(E\text{-}glass)})_5/(0_{(IMS60)})]_S$ HFRP specimens were also higher than that of the IMS60 CFRP specimen.

The term "hybrid effect" was coined to describe this synergetic effect. It is defined as the relative increase in the failure strain of the CFRP in an HFRP relative to the failure strain in an all-CFRP. Similar results of hybrid composites in which a phenomenon termed the "hybrid effect" have also been observed in some literature[18–21]. The hybrid effect, *HE*, can be calculated as

$$HE = \frac{\varepsilon_{f(HFRP)} - \varepsilon_{f(IMS60)}}{\varepsilon_{f(IMS60)}} \quad (8)$$

The hybrid ratio was not a sufficient parameter to explain and compare the hybrid effect in some reported literature because the hybrid ratio was the volume fraction ratio of FRP. The potential energy-based hybrid parameter was proposed as

$$HP = \frac{E_{(IMS60)}}{E_{HFRP}} \left(\frac{\varepsilon_{f(E-glass)}}{\varepsilon_{f(IMS60)}} \right)^2 \quad (9)$$

Figure 3 shows the relation between the *HE* of the HFRP specimens and the *HP*. Some reported experimental results[6–8,15,11,18–21] are also shown in this figure. The experimental results in woven fabric (in-house) are indicated for PAN-based carbon (T300) woven fabric and E-glass woven fabric hybrid fiber-reinforced epoxy matrix composites (HFRP). HFRP laminates were produced using epoxy matrix-based woven fabric FRP prepreg material F6343B-05P (plain woven fabric (PW), fiber: T300, matrix: #2500) and E-glass-8H/epoxy (eight-harness-stain fabric (8H), fiber: E-glass, matrix: 130°C-cured-type epoxy). T300-PW (F6343B-05P) prepreg was supplied by Toray Industries, Inc., and E-glass (E-glass-8H/epoxy) prepreg was supplied by Arisawa Mfg. Co., Ltd. FRP prepregs with nominal thicknesses of 0.245 mm (F6343B-05P, FAW: 200 g/m^2, RC: 44%) and 0.263 mm (E-glass-8H/epoxy, FAW: 290 g/m^2, RC: 40%) were used. The fabrication process was the same as that in the current study. However, the prepreg sheets were pressed at 490 kPa and cured at 130°C for 4 h (the heating rate was 1°C/min) by an autoclave in the laboratory. The fiber orientations of the HFRP specimens were set to orthotropic with $[((0/90)_{(T300)})/((0/90)_{(E\text{-}glass)})]_S$, $[((0/90)_{(E\text{-}glass)})/((0/90)_{(T300)})]_S$, $[((0/90)_{(E\text{-}glass)})/((0/90)_{(T300)})_2]_S$, $[((0/90)_{(E\text{-}glass)})/((0/90)_{(T300)})_3]_S$, $[((0/90)_{(E\text{-}glass)})/((0/90)_{(T300)})_5]_S$, $[((0/90)_{(E\text{-}glass)})_2/((0/90)_{(T300)})]_S$, $[((0/90)_{(E\text{-}glass)})_3/((0/90)_{(T300)})]_S$, and $[((0/90)_{(E\text{-}glass)})_5/((0/90)_{(T300)})]_S$. Static test specimens and were the same as those in the study. For $HP < 20$, the hybrid effect linearly increased with increasing hybrid parameter. The hybrid effect tended to be close to a constant value for $HP > 20$. The *HP* is an effective parameter for evaluating the hybrid effect of HFRP specimens.

There is an appreciable scattering of tensile strength for these composites. The statistical distribution of strength values is usually described by the Weibull equation[22]. The two-parameter Weibull distribution is given by

$$P_F = 1 - \exp\left[-\left(\frac{\sigma_f}{\sigma_0} \right)^m \right] \quad (10)$$

where P_F is the cumulative probability of failure of a composite at applied tensile strength σ_f, m is the Weibull modulus (Weibull shape parameter) of the composite, and σ_0 is a Weibull scale parameter (characteristic stress). The cumulative probability of failure, P_F, under a particular stress is given by

$$P_F = \frac{i}{n+1} \tag{11}$$

where i is the number of composite specimens that have broken at or below a stress level and n is the total number of composite specimens tested.

Figure 4 shows the Weibull plots of the mono CFRP and GFRP and HFRP specimens. The Weibull moduli, m, for the mono CFRP and GFRP specimens were calculated to be 17.60 for the IM600 CFRP specimen and 12.15 for the E-glass GFRP specimen. m values for the HFRP specimens are shown in **Table 2** and **Supplementary Fig. S3**. m for the $[(0_{(IMS60)})/(0_{(E\text{-}glass)})]_S$ HFRP specimen was similar to that for the mono IM600 CFRP specimens, and m for the $[(0_{(E\text{-}glass)})/(0_{(IMS60)})]_S$, $[(0_{(E\text{-}glass)})/(0_{(IMS60)})_2]_S$, $[(0_{(E\text{-}glass)})/(0_{(IMS60)})_3]_S$, $[(0_{(E\text{-}glass)})/(0_{(IMS60)})_5]_S$, $[(0_{(E\text{-}glass)})_2/(0_{(IMS60)})]_S$, $[(0_{(E\text{-}glass)})_3/(0_{(IMS60)})]_S$, and $[(0_{(E\text{-}glass)})_5/(0_{(IMS60)})]_S$ HFRP specimens was higher than that for the mono CFRP and GFRP specimens. In particular, m for the $[(0_{(E\text{-}glass)})_2/(0_{(IMS60)})]_S$, $[(0_{(E\text{-}glass)})_3/(0_{(IMS60)})]_S$, and $[(0_{(E\text{-}glass)})_5/(0_{(IMS60)})]_S$ HFRP specimens showed higher values.

The results clearly show that the HFRP specimens, except for the $[(0_{(IMS60)})/(0_{(E\text{-}glass)})]_S$ HFRP specimen, improved the specimen Weibull moduli of tensile strength. The differences in m can be attributed to the nature and distribution of the flaws present in the specimens. It is well known that many defects, including voids, fiber breakage, and fiber misalignment [23], are known to be introduced into these types of laminates during manufacturing and subsequent treatment. Outer high-ductility E-glass GFRP hybridization reduced the effects of the strength-limiting defects of IM600 CFRP, which, in turn, improved the Weibull moduli of $[(0_{(E\text{-}glass)})/(0_{(IMS60)})]_S$, $[(0_{(E\text{-}glass)})/(0_{(IMS60)})_2]_S$, $[(0_{(E\text{-}glass)})/(0_{(IMS60)})_3]_S$, $[(0_{(E\text{-}glass)})/(0_{(IMS60)})_5]_S$, $[(0_{(E\text{-}glass)})_2/(0_{(IMS60)})]_S$, $[(0_{(E\text{-}glass)})_3/(0_{(IMS60)})]_S$, and $[(0_{(E\text{-}glass)})_5/(0_{(IMS60)})]_S$ HFRP specimens. In contrast, the failures of the inner high-ductility E-glass GFRP hybridized HFRP specimen were predominantly initiated by outer IM600 CFRP defects. Hybridization effects are less likely to appear. Consequently, the $[(0_{(IMS60)})/(0_{(E\text{-}glass)})]_S$ HFRP specimen did not improve the Weibull modulus of the IM600 CFRP specimens.

The HFRP specimens showed a complicated shape, indicating a higher Weibull modulus. There is a clear Weibull modulus transition value in the hybrid ratio, hybrid parameter, tensile modulus, and strength.

The *S–N* curves for the mono $(0_{(IMS60)})_4$ CFRP and $(0_{(E\text{-}glass)})_4$ GFRP specimens can be described by a power law model. The power law model[24] is given by

$$\sigma_{max} = a \cdot \left(N_f\right)^b \tag{12}$$

where a and b are experimental constants. The least squares fitting of the fatigue trends with the power law model is illustrated in **Fig. 2**. The intercept, a, and slope, b, are calculated to be 3.292 and −0.0356 for the CFRP and 1.884 and −0.0899 for the GFRP, respectively.

The *S–N* curves of the CFRP- and GFRP-dominant behaviors in the HFRP specimens were calculated using the power law model of the CFRP and GFRP specimens and a simple rule of mixtures. The estimated results are also shown in **Fig. 2** and **Supplementary Fig. S4**.

The CFRP-dominant behaviour of the fatigue properties for the $[(0_{(IMS60)})/(0_{(E\text{-}glass)})]_S$ and $[(0_{(E\text{-}glass)})/(0_{(IMS60)})]_S$ HFRP specimens was higher than that of the estimated results. The GFRP-dominant behaviour of the fatigue properties for the $[(0_{(IMS60)})/(0_{(E\text{-}glass)})]_S$ and $[(0_{(E\text{-}glass)})/(0_{(IMS60)})]_S$ HFRP specimens was higher and lower, respectively, than that of the estimated results. The fatigue properties of the $[(0_{(IMS60)})/(0_{(E\text{-}glass)})]_S$ HFRP specimen were approximately 5% higher than those of the $[(0_{(E\text{-}glass)})/(0_{(IMS60)})]_S$ HFRP specimen. For the $[(0_{(E\text{-}glass)})/(0_{(IMS60)})]_S$, $[(0_{(E\text{-}glass)})/(0_{(IMS60)})_2]_S$, $[(0_{(E\text{-}glass)})/(0_{(IMS60)})_3]_S$, and $[(0_{(E\text{-}glass)})/(0_{(IMS60)})_5]_S$ HFRP specimens, the CFRP-dominant behaviour of the fatigue properties decreased with increasing volume fraction of CFRP, and the GFRP-dominant behaviour, which was lower than that of the estimated results, decreased with increasing volume fraction of CFRP. The CFRP-dominant behaviour of the fatigue properties for the $[(0_{(E\text{-}glass)})/(0_{(IMS60)})_5]_S$ HFRP specimen was lower than that of the estimated results. On the other hand, for the $[(0_{(E\text{-}glass)})/(0_{(IMS60)})]_S$, $[(0_{(E\text{-}glass)})_2/(0_{(IMS60)})]_S$, $[(0_{(E\text{-}glass)})_3/(0_{(IMS60)})]_S$, and $[(0_{(E\text{-}glass)})_5/(0_{(IMS60)})]_S$ HFRP specimens, the CFRP-dominant behaviour of fatigue properties, which was higher than the estimated results, decreased with increasing volume fraction of CFRP. For the same specimens, the GFRP-dominant behaviour, which was lower than the estimated results, increased with increasing volume fraction of CFRP.

Fatigue damage, such as matrix cracking and delamination, often results in a significant reduction in the modulus of composite laminates. Hence, it is crucial to develop an analytical model to describe the cumulative damage of composites due to fatigue based on apparent stiffness reduction[25–29]. **Figure 5** shows apparent stiffness reduction during fatigue loading (low, middle, and high stress levels) for the mono CFRP and GFRP and HFRP specimens.

Most of the stiffness reduction occurred in the earlier stages of fatigue life, whereas the damage density increased steeply. The rate of stiffness degradation became very low as soon as the damage density reached a saturated value. The stiffness reduction trends of the $[(0_{(IMS60)})/(0_{(E\text{-}glass)})]_S$, $[(0_{(E\text{-}glass)})/(0_{(IMS60)})]_S$, $[(0_{(E\text{-}glass)})/(0_{(IMS60)})_2]_S$, $[(0_{(E\text{-}glass)})/(0_{(IMS60)})_3]_S$, and $[(0_{(E\text{-}glass)})/(0_{(IMS60)})_5]_S$ HFRP specimens were similar to those of the mono $(0_{(IMS60)})_4$ CFRP specimen. The stiffness reduction trends of the $[(0_{(E\text{-}glass)})_2/(0_{(IMS60)})]_S$, $[(0_{(E\text{-}glass)})_3/(0_{(IMS60)})]_S$, and $[(0_{(E\text{-}glass)})_5/(0_{(IMS60)})]_S$ HFRP specimens were similar to those of the

mono $(0_{(E\text{-}glass)})_4$ GFRP specimen.

Stiffness reduction reflects the damaged state under fatigue cycles after the distribution of damage for the mono CFRP and GFRP and HFRP specimens. The cumulative fatigue damage[25–29] for the mono CFRP and GFRP and HFRP specimens, D_i, is defined as

$$D_i = 1 - \frac{E_i}{E_0} \tag{13}$$

where E_0 and E_i represent the apparent stiffness at the first cycle and the i-th cycle, respectively.

Figure 6 shows the cumulative fatigue damage for the mono CFRP and GFRP and HFRP specimens as a function of the normalized number of cycles, N_i/N_f (N_i represents the *i-th* cycle), which is widely used in the literature[25–29].

The cumulative fatigue damage, D_i, for the mono CFRP and GFRP and HFRP specimens increased with increasing N_i/N_f. For the mono CFRP and GFRP and HFRP specimens, there exists a relationship between D_i and N_i/N_f, given by

$$\frac{N_i}{N_f} = C(D_i)^n \left\{ \frac{1-\left(\frac{e^{D_{th}}}{e^{D_i}}\right)^{m_1}}{1-\left(\frac{e^{D_i}}{e^{D_C}}\right)^{m_2}} \right\} \tag{14}$$

where C, n, m_1, and m_2 are experimental constants. D_{th} and D_C are the threshold and critical cumulative fatigue damages, respectively, and are assumed to be $D_{th} = 0$ and $D_C = 1$. The estimated relationship between D_i and N_i/N_f is also shown in **Fig. 6**. The experimental results showed reasonable agreement with the estimated relation obtained from Eq. (14). The apparent stiffness reduction during fatigue loading for the mono CFRP and GFRP and HFRP specimens was estimated using Eqs. (13) and (14), and these lines are also shown in **Fig. 5**. Here, the experimental results were found to agree well with the estimated lines. Therefore, Eq. (14) is effective for understanding the fatigue properties.

Methods

Materials

HFRP laminates were produced using an epoxy matrix-based unidirectional (UD) FRP prepreg material QC133-149A (fiber: IMS60, matrix: 133) and E-glass-UD/epoxy (fiber: E-glass, matrix: 180°C-cured-type epoxy). The IMS60 carbon fiber was a high-strength PAN-based carbon fiber, and the E-class glass fiber was an alumino-borosilicate glass fiber with less than 1% w/w alkali oxides. IMS60 (QC133-149A) prepreg was supplied by Toho Tenax Co., Ltd., and E-glass (E-glass-UD/epoxy) prepreg was supplied by Arisawa Mfg. Co., Ltd. All sheets were manufactured using conventional prepreg technology. FRP prepregs with nominal thicknesses of 0.142 mm (QC133-149A, fiber area weight (FAW): 145 g/m^2, resin content (RC): 35%) and 0.137 mm (E-glass-UD/epoxy, FAW: 170 g/m^2, RC: 35%) were used.

Specimen preparation

The prepreg sheets were cut into the appropriate size and fiber orientation. The sheets were placed on a vacuum molding board. HFRP laminates were made using a hand lay-up and vacuum bagging technique (no bleeder). The fibre orientations of the mono CFRP and GFRP specimens and the HFRP specimens were set to unidirectional with $(0_{(IMS60)})_4$ (subscript 4 means four layers and $(0_{(IMS60)}/0_{(IMS60)}/0_{(IMS60)}/0_{(IMS60)})$), $(0_{(E\text{-}glass)})_4$, $[(0_{(IMS60)})/(0_{(E\text{-}glass)})]_S$ (subscript S means symmetry and $[(0_{(IMS60)})/(0_{(E\text{-}glass)})/(0_{(E\text{-}glass)})/(0_{(IMS60)})]$), $[(0_{(E\text{-}glass)})/(0_{(IMS60)})]_S$, $[(0_{(E\text{-}glass)})/(0_{(IMS60)})_2]_S$, $[(0_{(E\text{-}glass)})/(0_{(IMS60)})_3]_S$, $[(0_{(E\text{-}glass)})/(0_{(IMS60)})_5]_S$, $[(0_{(E\text{-}glass)})_2/(0_{(IMS60)})]_S$, $[(0_{(E\text{-}glass)})_3/(0_{(IMS60)})]_S$, and $[(0_{(E\text{-}glass)})_5/(0_{(IMS60)})]_S$.

The fiber volume fractions of the mono CFRP and GFRP specimens and the HFRP specimens are listed in **Table 1**. The prepreg sheets were pressed at 490 kPa and cured at 180°C for 4 h (the heating rate was 1°C/min) using an autoclave (Ashida Mfg. Co., Ltd., ACA Series) in the laboratory.

The HFRP laminates were cut into rectangular straight-side tensile test specimens with dimensions of 200 mm in length (gage length, L, of 100 mm) and 10 mm in width. The fiber axis in the specimen was oriented in line with the length of the tensile test specimen (0° direction specimen). To remove the effect of stress concentrations caused by surface roughness from the edges, the edges of the tensile test specimens were polished to remove scratches. Thinner plain-woven fabric glass fiber-reinforced plastic (50 mm in length, 10 mm in width, and 1 mm in thickness) tapered tabs were affixed to the tensile test specimen to minimize damage from the grips on the tensile testing machine. Similar specimen preparation procedures of other hybrid composites have been observed in the reported literature[3–5].

Static test

Static tests of HFRP specimens were performed using a universal testing machine (Shimadzu, Autograph AG-series) with a load cell of 50 kN. The specimen was set up in the testing machine. A crosshead speed of 5.0 mm/min was applied, and all

tests were conducted under the laboratory environment at room temperature (at 23°C ± 3°C and 50% ± 5% relative humidity). Strain gauges were used to measure longitudinal strains. Ten specimens were tested for each individual type of FRP specimen. Similar static test procedures of other hybrid composites have been observed in the reported literature[3–5].

Fatigue test

Fatigue tests of HFRP specimens were conducted using a servo-hydraulic testing machine (Servopulser EHF-E05-20L, Shimadzu) with a 50-kN load cell at a frequency of 10 Hz under cyclic loading with a constant amplitude. The waveform of the cyclic loads was sinusoidal. The stress ratio, R, of the minimum stress to the maximum stress was 0.1. The fatigue tests were terminated after 1×10^7 cycles. All tests were conducted in the laboratory environment at room temperature (at 23°C ± 3°C and 50% ± 5% relative humidity). Strain gauges were used to measure longitudinal strains. Similar fatigue test procedures of other composites have been observed in the reported literature[30,31].

References

1. Fitzer, E. PAN-based carbon fibers-Present state and trend of the technology from the viewpoint of possibilities and limits to influence and to control the fiber properties by the process parameters. *Carbon* **27**, 621–645, DOI: https://doi.org/10.1016/0008-6223(89)90197-8 (1989).
2. Chand, S. Review-Carbon fibers for composites. *J. Mater. Sci.* **35**, 1303–1313, DOI: https://doi.org/10.1023/A:1004780301489 (2000).
3. Naito, K., Yang, J. M. & Kagawa, Y. Tensile properties of high strength polyacrylonitrile (PAN)-based and high modulus pitch-based hybrid carbon fibers-reinforced epoxy matrix composite. *J. Mater. Sci.* **47**, 2743–2751, DOI: https://doi.org/10.1007/s10853-011-6101-8 (2012).
4. Naito, K., Yang, J.M. & Kagawa, Y. Development of high modulus/high strength carbon fiber reinforced nanoparticle filled polyimide based multiscale hybrid composites. *Mater. Sci. Forum* **654-656**, 2620–2623, DOI: https://doi.org/10.4028/www.scientific.net/MSF.654-656.2620 (2010).
5. Naito, K. Tensile properties of polyacrylonitrile- and pitch-based hybrid carbon fiber/polyimide composites with some nanoparticles in the matrix. *J. Mater. Sci.* **48**, 4163–4176, DOI: https://doi.org/10.1007/s10853-013-7229-5 (2013)
6. Hayashi, T., Koyama, K., Yamazaki, A. & Kihira, M. Development of new material properties by hybrid composition (2nd Report). *Fukugo Zairyo (composite materials)* **1**, 21–25 (1972).
7. Bunsell, A. R. & Harris, B. Hybrid carbon and glass fibre composites. *Composites* **5**, 157–164, DOI: https://doi.org/10.1016/0010-4361(74)90107-4 (1974).
8. Phillips, L. N. The hybrid effect - does it exist?. *Composites* **7**, 7–8, DOI: https://doi.org/10.1016/0010-4361(76)90273-1 (1976).
9. Hardaker, K. M. & Richardson, M. O. W. Trends in hybrid composite technology. *Polym-Plast. Technol.* **15**, 169–182, DOI: https://doi.org/10.1080/03602558008070011 (1980).
10. Short, D. & Summerscales, J. Amplitude distribution acoustic emission signatures of unidirectional fibre composite hybrid materials. *Composites* **15**, 200–206, DOI: https://doi.org/10.1016/0010-4361(84)90275-1 (1984).
11. Manders, P. W. & Bader, M. G. The strength of hybrid glass/carbon fibre composites Part 1 Failure strain enhancement and failure mode. *J. Mater. Sci.* **16**, 2233–2245, DOI: https://doi.org/10.1007/BF00542386 (1981).
12. Swolfs, Y., Verpoest, I. & Gorbatikh, L. Tensile failure of hybrid composites: measuring, predicting and understanding. *IOP Conf. Ser.: Mater. Sci. Eng.* **139**, 012008, DOI: https://doi.org/10.1088/1757-899X/139/1/012008 (2016).
13. Swolfs, Y., Gorbatikh, L. & Verpoest, I. Fibre hybridization in polymer composites: A review. *Compos. A Appl. Sci. Manuf.* **67**, 181–200, DOI: https://doi.org/10.1016/j.compositesa.2014.08.027 (2014).
14. Wu, Z., Wang, X., Iwashita, K., Sasaki, T. & Hamaguchi, Y. Tensile fatigue behaviour of FRP and hybrid FRP sheets. *Compos. B Eng.* **41**, 396–402, DOI: https://doi.org/10.1016/j.compositesb.2010.02.001 (2010).
15. Marom, G., Fischer, S., Tuler, F. R. & Wagner, H. D. Hybrid effects in composites: Conditions for positive or negative effects versus rule-of-mixtures behaviour. *J. Mater. Sci.* **13**, 1419–1426, DOI: https://doi.org/10.1007/BF00553194 (1978).
16. Stevanovic, M. M. & Stecenko, T. B. Mechanical behaviour of carbon and glass hybrid fibre reinforced polyester composites. *J. Mater. Sci.* **27**, 941–946, DOI: https://doi.org/10.1007/BF01197646 (1992).
17. Yao, L., Li, W. B., Wang, N., Li, W., Guo, X. & Qiu, Y. P. Tensile, impact and dielectric properties of three dimensional orthogonal aramid/glass fiber hybrid composites. *J. Mater. Sci.* **42**, 6494–6500, DOI: https://doi.org/10.1007/s10853-007-1534-9 (2007).

18. You, Y. J., Park, Y. H., Kim, H. Y. & Park, J. S. Hybrid effect on tensile properties of FRP rods with various material compositions. *Comps. Struct.* **80**, 117–122, DOI: https://doi.org/10.1016/j.compstruct.2006.04.065 (2007).

19. Pandya, K. S., Veerraju, C. & Naik, N. K. Hybrid composites made of carbon and glass woven fabrics under quasi-static loading. *Mater. Des.* **32**, 4094–4099, DOI: https://doi.org/10.1016/j.matdes.2011.03.003 (2011).

20. Zhang, J., Chaisombat, K., He, S. & Wang, C. H. Hybrid composite laminates reinforced with glass/carbon woven fabrics for lightweight load bearing structures. *Mater. Des.* **36**, 75–80, DOI: https://doi.org/10.1016/j.matdes.2011.11.006 (2012).

21. Czél, G. & Wisnom, M. Demonstration of pseudo-ductility in high performance glass/epoxy composites by hybridization with thin-ply carbon prepreg. *Compos. A Appl. Sci. Manuf.* **52**, 23–30, DOI: https://doi.org/10.1016/j.compositesa.2013.04.006 (2013).

22. Weibull, W. A statistical distribution function of wide applicability. *J. Appl. Mech.* **18**, 293–297 (1951).

23. Qiu, Y. & Schwartz, P. Micromechanical behavior of Kevlar-149/S-glass hybrid seven-fiber microcomposites. II: Stochastic modeling of stress-rupture of hybrid composites. *Compos. Sci. Technol.* **47**, 303–315, DOI: https://doi.org/10.1016/0266-3538(93)90038-I (1993).

24. Shiino, M. Y., de Siqueira, G. S. M., Cioffi, M. O. H., Montoro, S. R. & Donadon, M. V. Hygrothermal effect on composites under in-plane fatigue at stress ratios of R = −1 and R = 0.1: An analysis of quasi-isotropic stitched carbon fibers. *J. Mater. Eng. Perform.* **27**, 5964–5972, DOI: https://doi.org/10.1007/s11665-018-3584-3 (2018).

25. Ospina Cadavid, M., Al-Khudairi, O., Hadavinia, H., Goodwin, D. & Liaghat, G. H. Experimental studies of stiffness degradation and dissipated energy in glass fibre reinforced polymer composite under fatigue loading. *Polym. Polym. Compos.* **25**, 435–446, DOI: https://doi.org/10.1177/096739111702500602 (2017).

26. Yao, W. X. & Himmel, N. A new cumulative fatigue damage model for fibre-reinforced plastics. *Compos. Sci. Technol.* **60**, 59–64, DOI: https://doi.org/10.1016/S0266-3538(99)00100-1 (2009).

27. Epaarachchi, J. A. & Clausen, P. D. A new cumulative fatigue damage model for glass fibre reinforced plastic composites under step/discrete loading. *Compos. A Appl. Sci. Manuf.* **36**, 1236–1245, DOI: https://doi.org/10.1016/j.compositesa.2005.01.021 (2005).

28. Flore, D. & Wegener, K. Modelling the mean stress effect on fatigue life of fibre reinforced plastics. *Int. J. Fatigue* **82**, 689–699, DOI: https://doi.org/10.1016/j.ijfatigue.2015.09.027 (2016).

29. Stojković, N., Folić, R. & Pasternak, H. Mathematical model for the prediction of strength degradation of composites subjected to constant amplitude fatigue. *Int. J. Fatigue* **103**, 478–487, DOI: https://doi.org/10.1016/j.ijfatigue.2017.06.032 (2017).

30. Naito, K. & Oguma, H. Tensile properties of novel carbon/glass hybrid thermoplastic composite rods under static and fatigue loading. *Rev. Mater.* **22**, e-11843, DOI: https://doi.org/10.1590/S1517-707620170002.0176 (2017).

31. Naito, K. Flexural properties of carbon/glass hybrid thermoplastic epoxy composite rods under static and fatigue loadings. *Appl. Compos. Mater.* **28**, 753-766, DOI: https://doi.org/10.1007/s10443-021-09893-z (2021).

Author contributions statement

Kimiyoshi Naito: Data curation, Conceptualization, Methodology, Visualization, Software, Formal analysis, Investigation, Resources, Supervision, Validation, Writing - original draft, Writing - review & editing.

Additional information

Supplementary Information

Supplementary Information accompanies this paper.

Competing financial interests

The author declared no potential conflicts of interest with respect to the research, authorship and/or publication of this article.

Figure legends

Figure 1. Typical tensile stress–strain curves for the mono CFRP and GFRP and HFRP specimens.

Figure 2. Relation between the applied maximum stress and the number of cycles to failure, *S–N* curves, for the HFRP specimens. (a) $[(0_{(IMS60)})/(0_{(E\text{-}glass)})]_S$, (b) $[(0_{(E\text{-}glass)})/(0_{(IMS60)})]_S$, (c) $[(0_{(E\text{-}glass)})/(0_{(IMS60)})_2]_S$, (d) $[(0_{(E\text{-}glass)})/(0_{(IMS60)})_3]_S$, (e) $[(0_{(E\text{-}glass)})/(0_{(IMS60)})_5]_S$, (f) $[(0_{(E\text{-}glass)})_2/(0_{(IMS60)})]_S$, (g) $[(0_{(E\text{-}glass)})_3/(0_{(IMS60)})]_S$, and (h) $[(0_{(E\text{-}glass)})_5/(0_{(IMS60)})]_S$.

Figure 3. Relation between the hybrid effect of the HFRP specimens and the hybrid parameter.

Figure 4. Weibull plots of the mono CFRP and GFRP and HFRP specimens.

Figure 5. Stiffness reduction for the mono CFRP and GFRP and HFRP specimens. (a) $[(0_{(IMS60)})/(0_{(E\text{-}glass)})]_S$, (b) $[(0_{(E\text{-}glass)})/(0_{(IMS60)})]_S$, (c) $[(0_{(E\text{-}glass)})/(0_{(IMS60)})_2]_S$, (d) $[(0_{(E\text{-}glass)})/(0_{(IMS60)})_3]_S$, (e) $[(0_{(E\text{-}glass)})/(0_{(IMS60)})_5]_S$, (f) $[(0_{(E\text{-}glass)})_2/(0_{(IMS60)})]_S$, (g) $[(0_{(E\text{-}glass)})_3/(0_{(IMS60)})]_S$, (h) $[(0_{(E\text{-}glass)})_5/(0_{(IMS60)})]_S$, (i) $(0_{(IMS60)})_4$, and (j) $(0_{(E\text{-}glass)})_4$.

Figure 6. Cumulative fatigue damage for the mono CFRP and GFRP and HFRP specimens as a function of the normalized number of cycles. (a) $[(0_{(IMS60)})/(0_{(E\text{-}glass)})]_S$, $[(0_{(E\text{-}glass)})/(0_{(IMS60)})]_S$, $[(0_{(E\text{-}glass)})/(0_{(IMS60)})_2]_S$, $[(0_{(E\text{-}glass)})/(0_{(IMS60)})_3]_S$, $[(0_{(E\text{-}glass)})/(0_{(IMS60)})_5]_S$, and $(0_{(IMS60)})_4$, and (b) $[(0_{(E\text{-}glass)})_2/(0_{(IMS60)})]_S$, $[(0_{(E\text{-}glass)})_3/(0_{(IMS60)})]_S$, $[(0_{(E\text{-}glass)})_5/(0_{(IMS60)})]_S$, and $(0_{(E\text{-}glass)})_4$.

Figures

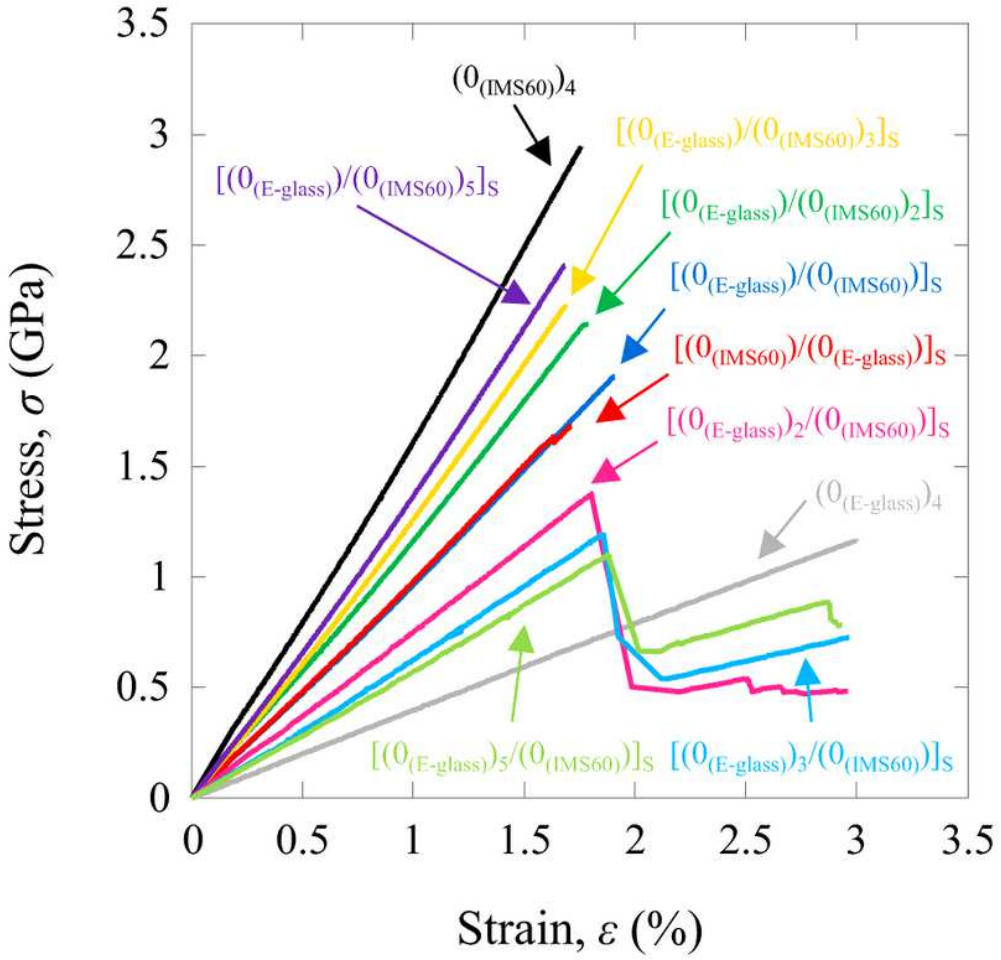

Figure 1

Typical tensile stress–strain curves for the mono CFRP and GFRP and HFRP specimens.

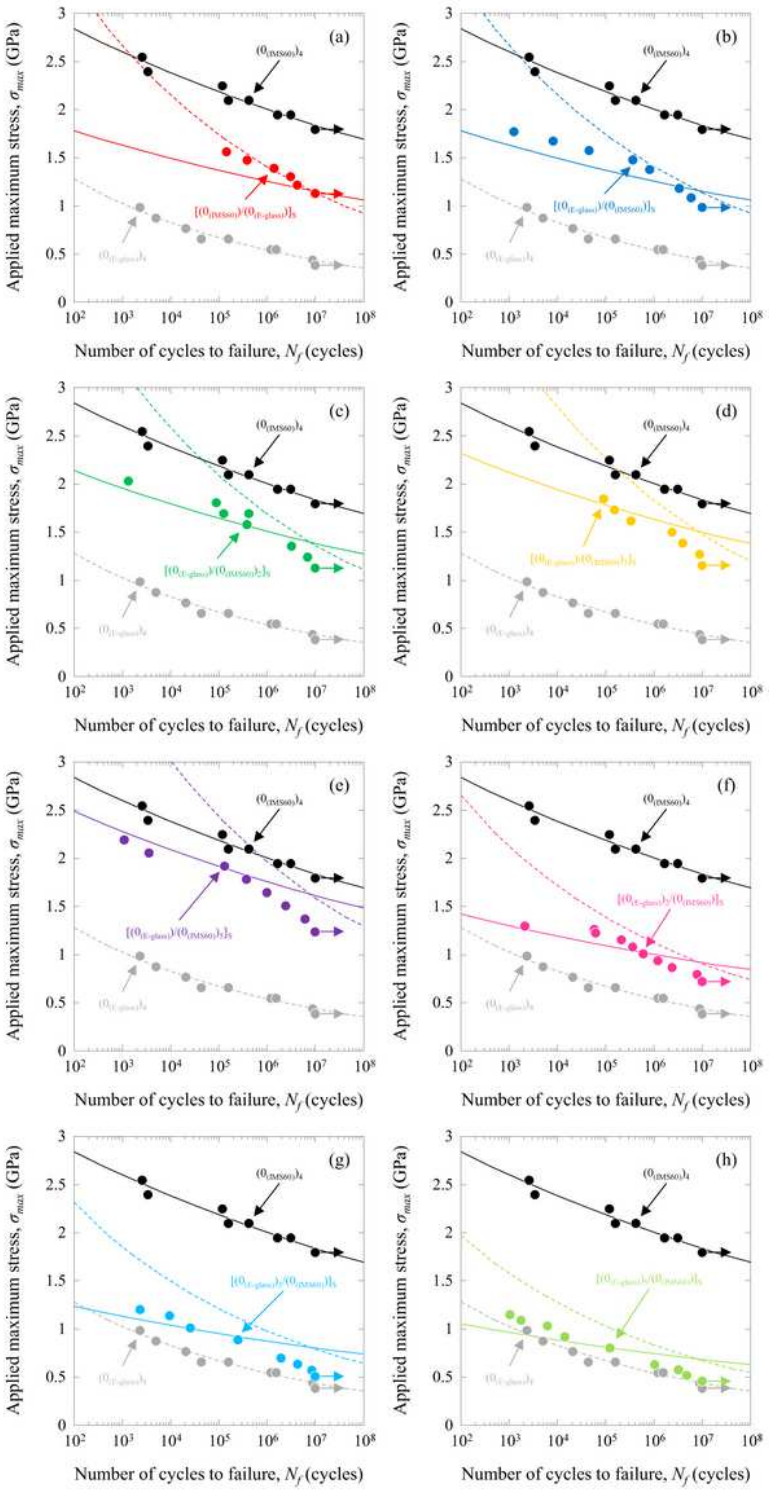

Figure 2

Relation between the applied maximum stress and the number of cycles to failure, S–N curves, for the HFRP specimens. (a) [(0(IMS60))/(0(E-glass))]S, (b) [(0(E-glass))/(0(IMS60))]S, (c) [(0(E-glass))/(0(IMS60))2]S, (d) [(0(E-glass))/(0(IMS60))3]S, (e) [(0(E-glass))/(0(IMS60))5]S, (f) [(0(E-glass))2/(0(IMS60))]S, (g) [(0(E-glass))3/(0(IMS60))]S, and (h) [(0(E-glass))5/(0(IMS60))]S.

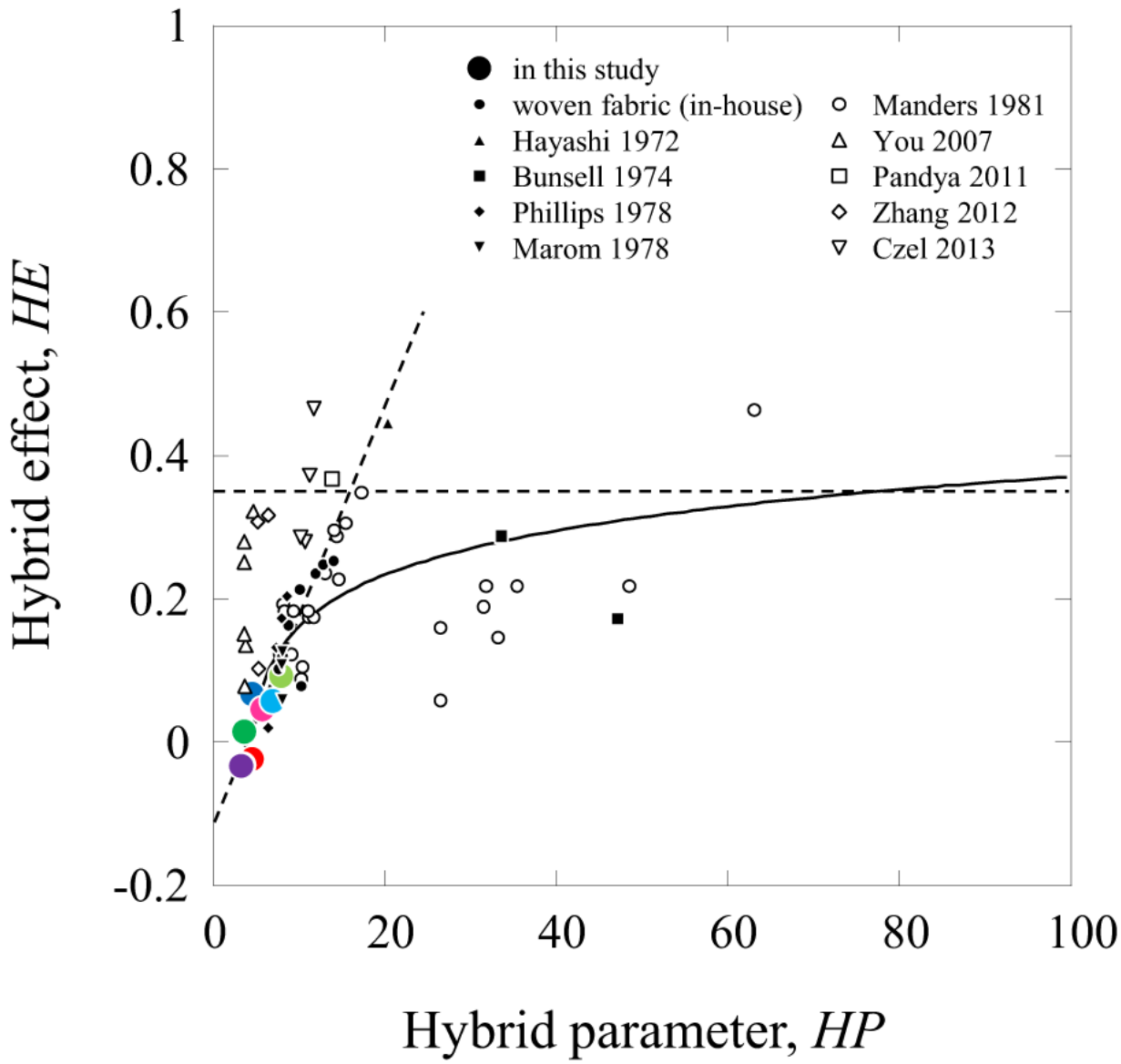

Figure 3

Relation between the hybrid effect of the HFRP specimens and the hybrid parameter.

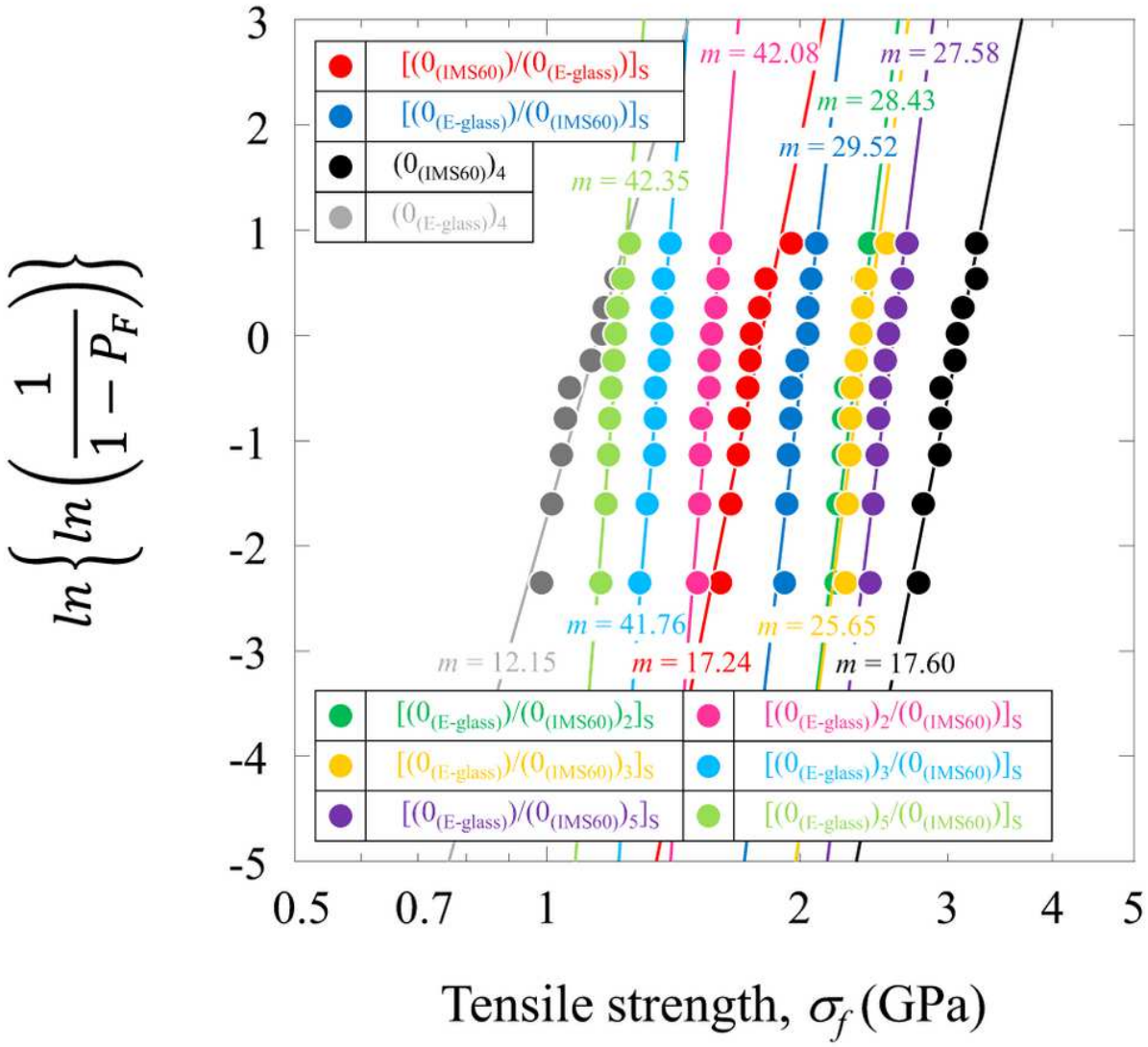

Figure 4

Weibull plots of the mono CFRP and GFRP and HFRP specimens.

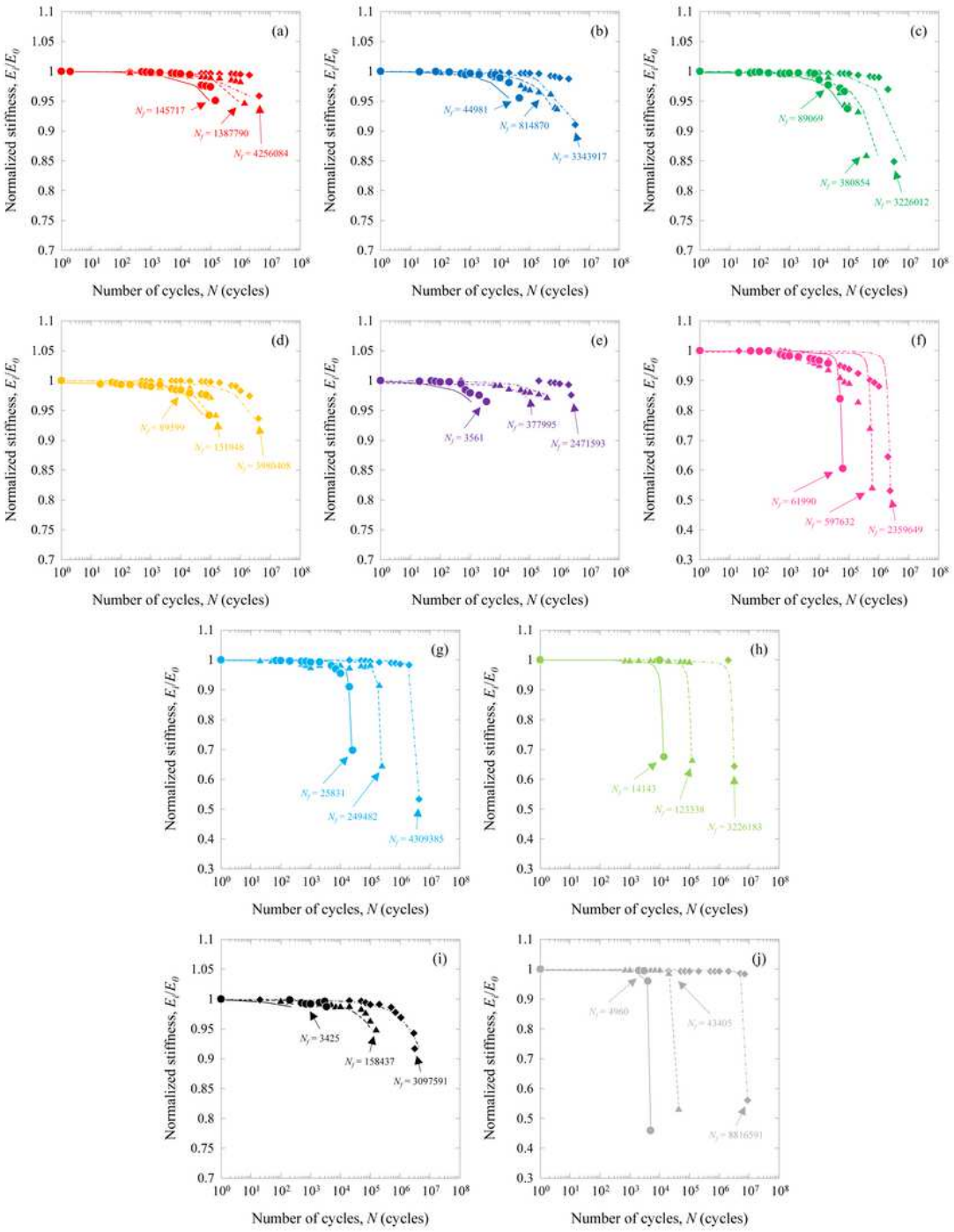

Figure 5

Stiffness reduction for the mono CFRP and GFRP and HFRP specimens. (a) [(0(IMS60))/(0(E-glass))]S, (b) [(0(E-glass))/(0(IMS60))]S, (c) [(0(E-glass))/(0(IMS60))2]S, (d) [(0(E-glass))/(0(IMS60))3]S, (e) [(0(E-glass))/(0(IMS60))5]S, (f) [(0(E-glass))2/(0(IMS60))]S, (g) [(0(E-glass))3/(0(IMS60))]S, (h) [(0(E-glass))5/(0(IMS60))]S, (i) (0(IMS60))4, and (j) (0(E-glass))4.

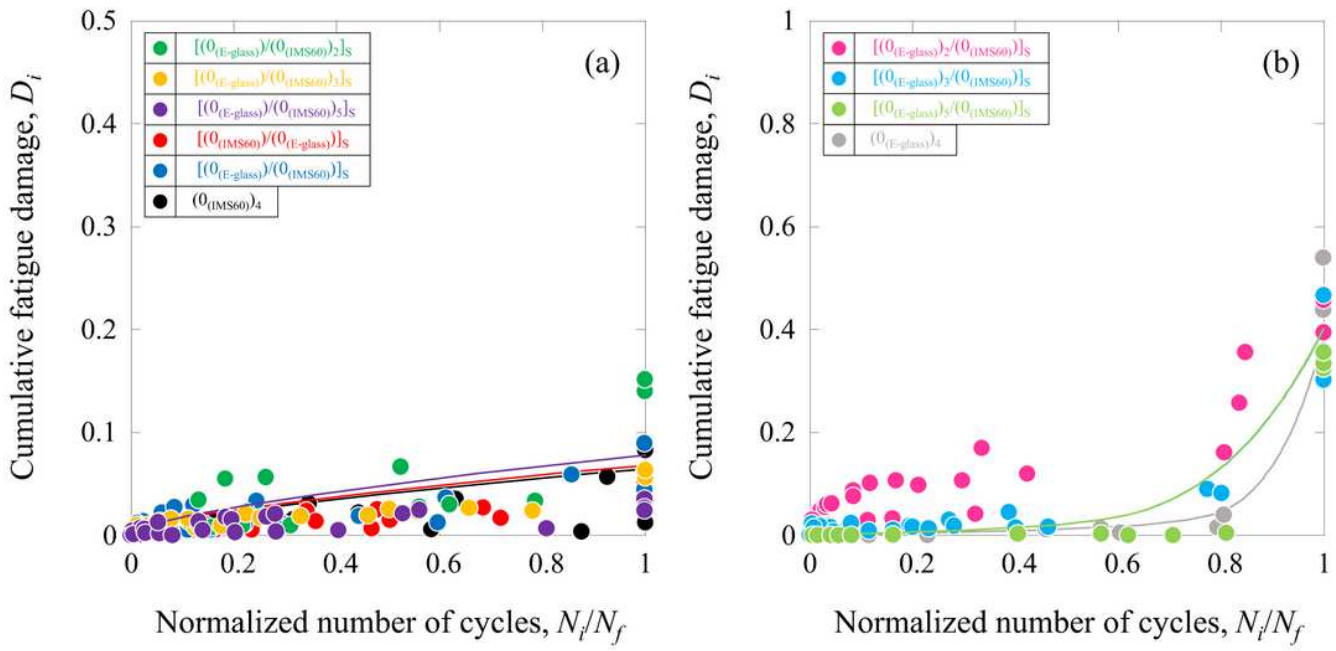

Figure 6

Cumulative fatigue damage for the mono CFRP and GFRP and HFRP specimens as a function of the normalized number of cycles. (a) [(0(IMS60))/(0(E-glass))]S, [(0(E-glass))/(0(IMS60))]S, [(0(E-glass))/(0(IMS60))2]S, [(0(E-glass))/(0(IMS60))3]S, [(0(E-glass))/(0(IMS60))5]S, and (0(IMS60))4, and (b) [(0(E-glass))2/(0(IMS60))]S, [(0(E-glass))3/(0(IMS60))]S, [(0(E-glass))5/(0(IMS60))]S, and (0(E-glass))4.

Supplementary Files

This is a list of supplementary files associated with this preprint. Click to download.

- SupplementaryInformationSR.docx